Spectrophotometric Reverberation Mapping of Intermediate-mass Black Hole NGC 4395

Shivangi Pandey[1,2] , Suvendu Rakshit[1] , Krishan Chand[3], C. S. Stalin[4] , Hojin Cho[5] , Jong-Hak Woo[5] , Priyanka Jalan[6],
Amit Kumar Mandal[6,7] , Amitesh Omar[8], Jincen Jose[1,9], and Archana Gupta[2]

[1] Aryabhatta Research Institute of Observational Sciences, Nainital–263001, Uttarakhand, India; Shivangipandey@aries.res.in, suvenduat@gmail.com
[2] Department of Applied Physics/Physics, Mahatma Jyotiba Phule Rohilkhand University, Bareilly–243006, India
[3] Department of Physics and Astronomical Science, Central University of Himachal Pradesh, Dharamshala, Kangra–176215, Himachal Pradesh, India
[4] Indian Institute of Astrophysics, Block II, Koramangala, Bangalore–560034, India
[5] Department of Physics & Astronomy, Seoul National University, Seoul–08826, Republic of Korea
[6] Center for Theoretical Physics of the Polish Academy of Sciences, Al. Lotników 32/46, 02-668 Warsaw, Poland
[7] Astronomy Program, Department of Physics and Astronomy, Seoul National University, Seoul–08826, Republic of Korea
[8] Indian Institute of Technology Kanpur, Kanpur–208016, Uttar Pradesh, India
[9] Center for Basic Sciences, Pt. Ravishankar Shukla University, Raipur, Chhattisgarh–492010, India
Received 2024 June 14; revised 2024 September 23; accepted 2024 September 24; published 2024 November 15

Abstract

Understanding the origins of massive black hole seeds and their coevolution with their host galaxy requires studying intermediate-mass black holes (IMBHs) and estimating their mass. However, measuring the masses of these IMBHs is challenging, due to the high-spatial-resolution requirement. Spectrophotometric reverberation monitoring is performed for a low-luminosity Seyfert 1 galaxy, NGC 4395, to measure the size of the broad-line region and black hole mass. The data were collected using the 1.3 m Devasthal fast optical telescope and 3.6 m Devasthal optical telescope at ARIES, Nainital, over two consecutive days in 2022 March. The analysis revealed strong emission lines in the spectra and light curves of the merged 5100 Å spectroscopic continuum flux (f_{5100}) with the photometric continuum V band and Hα, with fractional variabilities of 6.38% and 6.31% respectively. In comparison to several previous studies with lag estimation <90 minutes, our calculated Hα lag supersedes them by $125.0^{+6.2}_{-6.1}$ minutes, using the ICCF and JAVELIN methods. The velocity dispersion (σ_{line}) of the broad-line clouds is measured to be $544.7^{+22.4}_{-25.1}$ km s^{-1}, yielding a black hole mass of $\sim 2.2^{+0.2}_{-0.2} \times 10^4 M_\odot$ and an Eddington ratio of 0.06.

Unified Astronomy Thesaurus concepts: Black holes (162); Active galactic nuclei (16); Reverberation mapping (2019); Spectroscopy (1558); Intermediate-mass black holes (816)

Materials only available in the online version of record: machine-readable table

1. Introduction

Understanding the growth and evolution of supermassive black holes (SMBHs) formed in the early Universe is one of the most fundamental problems. Recent observations of JWST suggest the presence of massive black holes at $z > 7$, challenging the theories of black hole formation and evolution at the early Universe (e.g., V. Kokorev et al. 2023). The origin of these massive seeds is believed to be heavier-than-stellar-mass black holes of mass ranging between ~ 10–$100 M_\odot$. Hence, their progenitor is suggested to be intermediate-mass black holes (IMBHs) with masses 10^3–$10^6 M_\odot$, making them currently active research subjects (e.g., A. Loeb & F. A. Rasio 1994; M. A. Latif et al. 2013; J. E. Greene et al. 2020). However, the detection of IMBHs is challenging, mainly due to their low luminosity and negligible variability (see M. Mezcua 2017; J. E. Greene et al. 2020), and very few candidates have been known so far (e.g., J. E. Greene & L. C. Ho 2004, 2007; A. E. Reines et al. 2013; L. Shin et al. 2022; C. Ward et al. 2022; X. Yang et al. 2022; S. DiRenzo et al. 2024).

The study of the mass distribution and coevolution of black holes and their host galaxies is enabled by the correlation between the black hole mass and the stellar velocity dispersion $\sigma_\star$ of the

bulge of the galaxy (see J. Hu 2008; J. H. Woo et al. 2015), as identified by J. Kormendy & L. C. Ho (2013). It is beyond the capability of modern instruments to spatially resolve the central engines of active galactic nuclei (AGNs; however, see the recent results from Gravity Collaboration et al. 2018; GRAVITY Collaboration et al. 2020; A. Amorim et al. 2021; R. Abuter et al. 2024), hampering accurate measurements of their black hole masses. Consequently, most of the studies on the central engines of AGNs are based on reverberation mapping (RM; B. M. Peterson 1993). RM observes the response of emission lines to continuum variations from the central source, thus studying the size and structure of the broad-line region (BLR). This method has been applied to more than 100 objects (e.g., B. M. Peterson 1993, 1998, 2002, 2004, 2014; S. Kaspi et al. 2000, 2007; M. Dietrich et al. 2012; M. C. Bentz et al. 2013; P. Du et al. 2014, 2015, 2016, 2018; J. H. Woo et al. 2015, 2024; C. J. Grier et al. 2017; L. Pei et al. 2017; M. M. Fausnaugh et al. 2017; S. Park et al. 2017; S. Rakshit et al. 2019, 2020; E. D. Bontà et al. 2020; P. R. Williams et al. 2020; E. M. Cackett et al. 2021; C. Hu et al. 2021; S.-S. Li et al. 2021; S. Pandey et al. 2022; V. U et al. 2022; U. Malik et al. 2023). Unfortunately, only very few RM-based studies have been conducted for IMBHs, due to low variability (see B. M. Peterson et al. 2005; S. E. Rafter et al. 2011; H. Cho et al. 2021).

NGC 4395 is a low-luminosity Seyfert 1 galaxy with strong emission lines at a redshift of 0.001, hosting an IMBH candidate (A. V. Filippenko & L. C. Ho 2003). It contains the least-luminous broad-lined AGN known to date, with a

bolometric luminosity lower than $10^{41}\,\mathrm{erg\,s^{-1}}$ and stellar mass $\sim 10^9 M_\odot$ (H. Cho et al. 2021; A. V. Filippenko & L. C. Ho 2003, 2003). The Eddington ratio of NGC 4395 is $\sim 5\%$ (J.-H. Woo et al. 2019), comparable to that of other RM AGNs. Therefore, this galaxy provides a unique opportunity to investigate photoionization and size–luminosity relations at the extreme-low-luminosity regime of AGNs. The exact mass of the central black hole of NGC 4395 is in conflict, with estimates ranging from $9 \times 10^3 M_\odot$ to $4 \times 10^5 M_\odot$ (e.g., A. V. Filippenko & L. C. Ho 2003; B. M. Peterson et al. 2005; H. Edri et al. 2012; J.-H. Woo et al. 2019).

Measuring an emission-line lag for NGC 4395 has been challenging due to low continuum variation and the variable component being weak for emission lines such as He II, Hγ, and mostly for Hβ. However, various attempts have been made for lag measurement, such as for Hα (L.-B. Desroches et al. 2006; H. Edri et al. 2012; J.-H. Woo et al. 2019; H. Cho et al. 2020, 2021), for Hβ (H. Edri et al. 2012), for Paβ (F. La Franca et al. 2015), and for C IV (B. M. Peterson et al. 2005). J.-H. Woo et al. (2019) provided the first reliable Hα lag of 83 ± 14 minutes using photometric RM (PRM), which, combined with the line width of $426 \pm 2.5\,\mathrm{km\,s^{-1}}$ from a single-epoch spectrum, leads to a black hole mass estimate of $10{,}000 M_\odot$. However, the photometric Hα filter has a continuum contribution that can be a significant source of uncertainty in estimating a true lag. Therefore, quantifying the continuum variability and contribution in the Hα filter is crucial. A further PRM attempt was made by H. Cho et al. (2020), through extensive photometric monitoring campaigns, where the authors employed various scaling parameter values to correct the continuum contribution in the Hα narrowband filter. The lag value was found to have a large range, from 55 to 122 minutes, when the Hα narrowband flux was corrected for continuum, assuming this contribution to be 0%–100% of V-band variability. In spectroscopic RM, such correction is not needed, as flux-calibrated spectra provide the continuum variation, which can be measured by modeling it with a power law alongside decomposed emission lines. Therefore, spectroscopic RM is crucial to estimating BLR size and calibrating the size–luminosity relation of the extremely-low-luminosity region and accurate black hole mass.

Previous attempts at spectroscopic RM have either been inconclusive or provided a lag upper limit. H. Cho et al. (2021) made a noteworthy attempt, using high-cadence imaging data for NGC 4395. As a follow-up to previous PRM (J.-H. Woo et al. 2019; H. Cho et al. 2020), they provided an improved Hα line dispersion measurement. However, due to the lack of variability in the light curve and bad weather losses, only a lag upper limit of less than 3 hr has been provided. To measure BLR size and black hole mass using spectroscopic RM of this low-luminosity Seyfert 1 galaxy, NGC 4395, we conducted a comprehensive photometric and spectroscopic monitoring program for two consecutive nights. In this paper, we present the result of this monitoring program measuring the BLR size and black hole mass.

The paper is organized as follows. The observations and data reduction are discussed in Section 2. The results and analysis are presented in Section 3. The measurement of the black hole mass and a few important aspects are discussed in Section 4, and finally a conclusion is presented in Section 5.

2. Observations and Data Reduction

NGC 4395 was observed using two telescopes hosted and operated by the Aryabhatta Research Institute of Observational Sciences (ARIES), Nainital, India, from 2022 March 10 to 11, with observations spanning 7–8 hr on both nights, which exceeds the expected lag of the source by multiple times.

(I) Photometric observations were conducted using the 1.3 m Devasthal fast optical telescope (DFOT; R. Sagar et al. 2011), equipped with a 2k × 2k CCD camera providing a plate scale of $0\rlap{.}''53\,\mathrm{pixel^{-1}}$. The source NGC 4395 was observed in the V band and narrowband filters Hα and [S II], with exposures of 300 s in the sequence V–Hα–[S II]. Consequently, the source was observed in all three filters with a 10 minutes cadence. Approximately 42 photometric data points were obtained in the V band. In this work, the V-band photometry results are presented. PRM results using narrowband Hα and [S II] data will be reported elsewhere.

(II) Spectroscopy of the source was performed using the 3.6 m Devasthal optical telescope (DOT; B. Kumar et al. 2018). The ARIES–Devasthal Faint Object Spectrograph and Camera (ADFOSC; A. Omar et al. 2019) mounted at the 3.6 m DOT was used for spectroscopic observations. It is comprised of a 4k × 4k deep-depletion CCD camera providing a $0\rlap{.}''2\,\mathrm{pixel^{-1}}$ scale with 2 × 2 binning (D. Panchal et al. 2023). The spectroscopic observation was carried out with a slit $3\rlap{.}''2$ wide and $8''$ long and a $132R-600\,\mathrm{gr\,mm^{-1}}$ grism that covers the wavelength range of 3500–7000 Å, centered at 4880 Å. Spectroscopic frames of 300 s duration were taken throughout the night, along with bias and flat frames for preprocessing. The seeing varied throughout the night, ranging from $0\rlap{.}''5$ to $1\rlap{.}''5$. The instrumental resolution was measured to be 7 Å (312 km s^{-1}), by modeling the emission lines present in the combined HgAr Ne lamp obtained in the same configuration as the source frame, and was also verified using skylines present in the observed spectrum of NGC 4395.

Detecting variability in the central engine of the low-luminosity NGC 4395 is difficult, due to the contribution from its extended host galaxy and narrow-line region (NLR). Considering the NLR is spatially resolved using ground-based telescopes, this leads to variable contributions in the slit spectra, which make the standard approach of relative flux calibration using narrow lines impractical (see H. Cho et al. 2021), making accurate flux calibration with respect to a reference star essential. For this purpose, the slit was oriented to encompass a nearby comparison star, as depicted in Figure 1. This allowed for the simultaneous acquisition of spectra for both the source and a steady comparison star. The number of photometric data points and spectra obtained from both telescopes are detailed in Table 1. Approximately 100 spectra were obtained from the 3.6 m DOT, sufficient for lag measurement through time-series analysis.

2.1. Differential Photometry

NGC 4395 is an extended spiral galaxy, with the core marked with a red circle, as shown in Figure 1, and the three steady comparison stars marked with white circles. These comparison stars are used to perform differential photometry. Initially, the images from the respective days were aligned using a Python package named Astroalign (M. Beroiz et al. 2020). The alignment ensured that the point-spread function (PSF) matched that of the image with the lowest resolution,
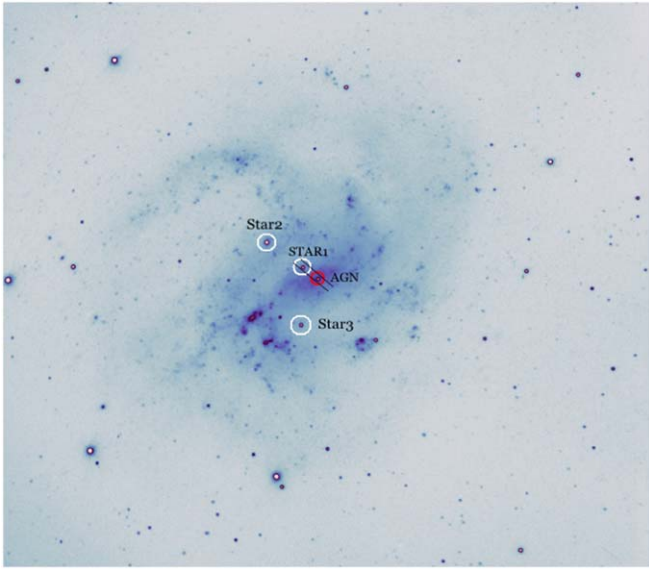
Figure 1. The combined *V*-band image of NGC 4395 obtained on 2022 March 10 using the 1.3 m DFOT. Three comparison stars are marked with white circles, while the target AGN is denoted with a red circle. The slit is oriented to cover both the AGN and a comparison star. The field of view is 66′ (18′ × 18′) for the 1.3 m DFOT.

Table 1
Photometric Observations Using the 1.3 m DFOT in the *V*-band Filter and Spectroscopic Observations from the 3.6 m DOT (ADFOSC) on 2022 March 10 and 11

Observation	Data	
	Photometric *V* Band (1.3 m DFOT)	Spectra (3.6 m DOT)
March 10	19	43
March 11	23	64

Note. Column (1): observation date. Column (2): number of data points observed from the 1.3 m DFOT. Column (3): spectral data obtained from the 3.6 m DOT.

resulting in frames with uniform PSF. The preprocessing stage involved cleaning the photometric frames, i.e., bias subtraction, flat-fielding, and cosmic-ray correction. Aperture photometry was carried out using a Python wrapper called SEP (K. Barbary 2016) for source extraction.

The aperture size was 2.5 times the average FWHM of all three comparison stars. The FWHM was calculated by fitting the Gaussian function. The sky contribution was assumed to be 4–5 times the FWHM. The differential magnitude of the source compared to the three comparison stars present in the same field was then calculated. Finally, the zero-point was added to convert the differential instrumental magnitude into the actual *V*-band magnitude. The light curve obtained from the 1.3 m DFOT in the *V* band on both days is depicted in Figure 3. The light curve is merged with the continuum flux at 5100 Å (f_{5100}) obtained from the spectra, as discussed in Section 2.2.

2.2. Spectroscopic Reduction and Flux Calibration

2.2.1. Spectroscopy

The spectroscopic reduction was performed using IRAF software (D. Tody 1986, 1993; National Optical Astronomy

Observatories 1999), encompassing bias subtraction, flat-fielding, and cosmic-ray removal with the L.A. cosmic algorithm (P. G. v. van Dokkum 2001). Flat correction was executed using a tungsten LED lamp, which was normalized. The bias-corrected frames, including the source and lamps, were divided by it. The apertures of the center of NGC 4395 and the comparison stars are extracted with a size of 4″ using the task "apall," which is included in the IRAF software. Additionally, HgAr and neon lamps were observed in the same configuration as the source frame, for wavelength calibration covering the wavelength range of 3500–7000 Å. Both of these lamps were combined using the "imcombine" task. The combined lamps were identified, and the final wavelength solution was applied to the source and reference star frames to complete the wavelength calibration process.

2.2.2. Flux Calibration

Accurate flux calibration is imperative for studying emission-line variability. In RM studies, narrow-line fluxes are typically relied upon for precise flux calibration, assuming that the narrow-line fluxes remain constant throughout the monitoring campaign. However, this assumption does not hold for NGC 4395, having an extended and resolved host galaxy and NLR. The flux contamination, in this case, depends upon the seeing variation and its variability throughout the monitoring campaign. Moreover, H. Cho et al. (2021) have identified significant variability from the narrow [S II] line fluxes in the slit-based spectroscopy. This renders the use of narrow-line fluxes for relative flux calibration unsuitable.

We follow the procedure outlined in H. Cho et al. (2021) for flux calibration. As the in-slit comparison star S1 is not a standard star, its slope and features were matched with HD 165341 (K0 V; hereafter $L1_{cat}$) from the Indo-US Library (similar to, H. Cho et al. 2021). The library spectrum S_{lib} was scaled to match the known magnitude of S1 from the Vizier Online Data Catalog (Gaia Collaboration 2020).[10] Subsequently, the scaled library spectrum ($S_{lib,scaled}$) was used to create a response function for flux calibration. To generate the response curve ($S_\star$), a polynomial function was fitted by considering the line-free region of the scaled library spectrum $S_{lib,scaled}$. Similarly, this process was repeated for star S1 epoch by epoch, denoted as $S1_i$. The sensitivity curve S_i was then calculated as $S_i = S_\star/S1_i$ for the *i*th epoch. Finally, the source wavelength-calibrated spectra were multiplied by the sensitivity function S_i, resulting in its flux calibration.

Finally, the flux-calibrated spectra obtained from the method above were recalibrated with *V*-band photometric data points acquired using the 1.3 m DFOT. Subsequently, the *V*-band magnitude was converted to flux density using the formula $V = 15 - 2.5 \log (F_\nu/3.64)$. This photometric *V*-band flux density was used to scale the integrated region 5400–5600 Å of the spectra, resulting in the final flux-calibrated spectra.

2.2.3. Spectral Decomposition

The publicly available multicomponent spectral fitting code PyQSOFit was used for decomposition and spectrum fitting, developed by H. Guo et al. (2018) and H. Guo (2023). A comprehensive description of the code and its applications can be found in H. Guo et al. (2019), Y. Shen et al. (2019), and
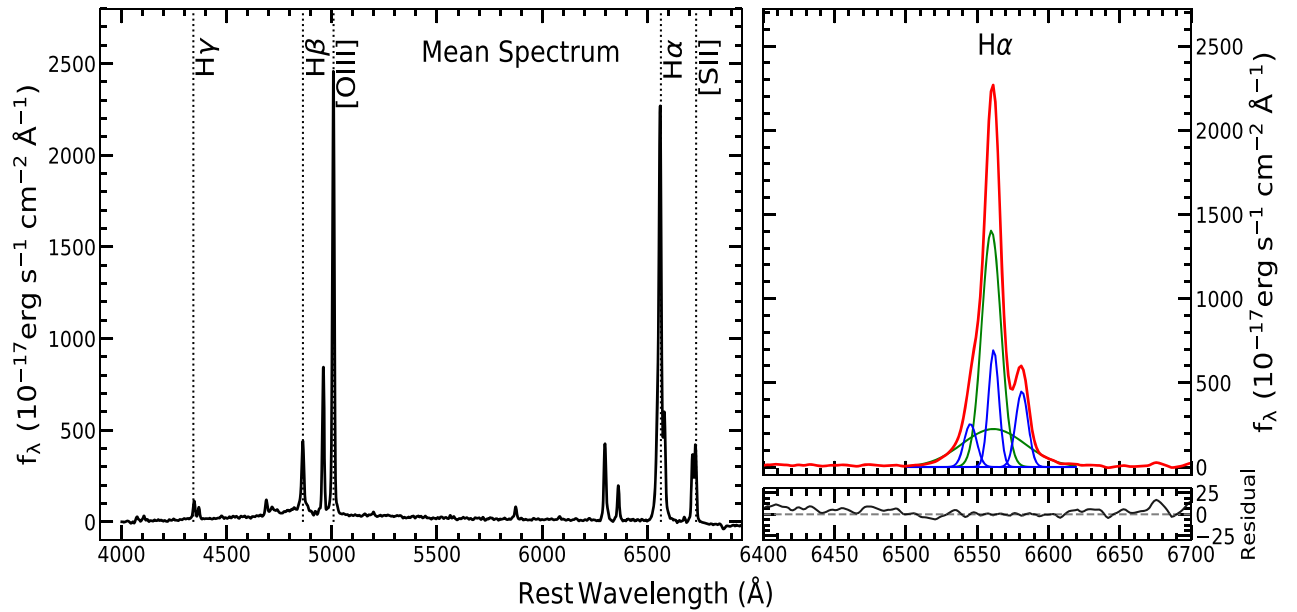
---

[10] http://vizier.cds.unistra.fr/viz-bin/VizieR-S?2MASS J12255090%2b3333100

Figure 2. An example of spectral decomposition of the mean spectrum of March 11. The left panel shows the mean spectrum with marked emission-line regions. The right panel presents the decomposition of the Hα component into narrow and broad components with narrow [N II] lines. The broad Hα component is modeled with the double Gaussian shown in green, and the narrow component is modeled with the single Gaussian shown in blue. The narrow [N II] λ6549 and λ6585 emission lines are shown with a single-Gaussian fit in blue. The total line construction is shown in red with the illustrated continuum region. The lower-right panel shows the residual of the fit in black.

S. Rakshit et al. (2020). Each AGN spectrum underwent correction for Galactic extinction, using the map by D. J. Schlegel et al. (1998) and the Milky Way extinction law of E. L. Fitzpatrick (1999) with $R_V = 3.1$. Subsequently, deredshifting was performed using the redshift ($z = 0.001$). Following this, the continuum was modeled using a power law in the line-free region of the spectrum and Fe II templates using T. A. Boroson & R. F. Green (1992). After subtracting the continuum, detailed multi-Gaussian modeling was conducted in the Hα region to fit the emission lines shown in Figure 2. The narrow Hα, [N II]λ6549, [NII]λ6585, [S II]λ6718, and [S II]λ6732 lines were modeled using a single Gaussian, with the velocity and velocity offset tied to each other. The broad Hα component was modeled with double Gaussians. The best-fit model was obtained via χ^2 minimization. Subsequently, the emission-line flux, width, and continuum luminosity at 5100 Å with a window of 20 Å on both sides were calculated from the best-fitting model.

Figure 2 presents an example of spectral fitting with PyQSOFit, where various emission lines are delineated, including broad and narrow emission-line components. Since the broad component of Hα emanates from the BLR, the broad Hα flux must be used to construct the emission-line light curve. However, due to the low–medium signal-to-noise ratios (S/Ns) of the spectra (i.e., S/Ns around 10 to 20 at continuum 6100–6200 Å), constraining the line wing is difficult, as it is prone to S/N. Hence, we used the best-fit broad Hα model profile obtained from the PyQSOFit fitting and integrated it in the wavelength range of 6500–6600 Å to create the Hα emission-line light curve, avoiding wings.

2.3. Generating a Light Curve

Due to the limited number of photometric data points on both nights, the spectroscopic flux at 5100 Å was used to augment the cadence in the continuum light curve. To mitigate

the systematic deviations introduced by merging two continuum light curves observed from different telescopes, both the photometric and f_{5100} light curves were intercalibrated using the Python module PyCALI,[11] as described in Y.-R. Li et al. (2014). PyCALI employs a damped random walk (DRW) with a Bayesian approach to model the intercalibrated light curves and estimates parameters such as the amplitude of variation (σ), timescale (τ), scale, and shift factors for intercalibrating the light curves.

The upper panel of Figure 3 illustrates the merged V-band photometric flux density and f_{5100} light curves. Additionally, the lower panel displays the Hα emission-line light curve on both nights. To mitigate noise, particularly in the Hα light curve, these light curves were smoothed by binning five continuous data points. The light curve data are shown in Table 2.

3. Analysis and Results

3.1. Variability

We find the fractional variability amplitude (F_{var}) for merging the photometric V band and spectroscopic optical continuum flux at 5100 Å (f_{5100}) using the following equation (P. M. Rodriguez-Pascual et al. 1997):

$$F_{\text{var}} = \frac{\sqrt{(\sigma^2 - \langle \sigma_{\text{err}}^2 \rangle)}}{\langle f \rangle}, \qquad (1)$$

where σ^2 is the variance, σ_{err}^2 is the mean square error, and $\langle f \rangle$ is the arithmetic mean of the light curves. The F_{var} for the merged continuum of March 10 is 2.6% and for March 11 it is 7%. For the entire light curve, including both days, it is 6.0%. The maximum variability for the Hα emission-line flux is 6.3% for two days.
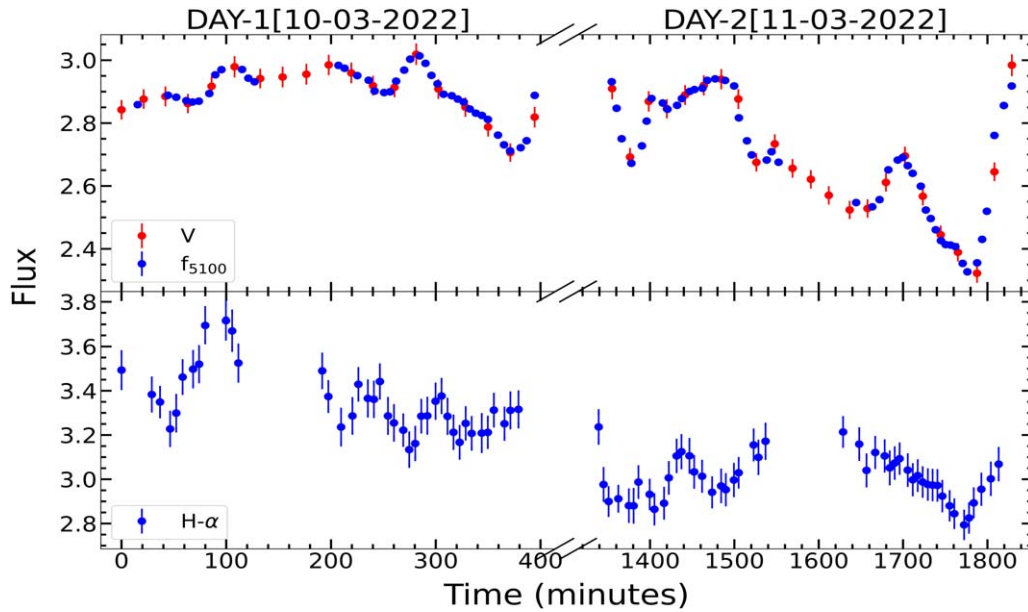
---

[11] https://github.com/LiyrAstroph/PyCALI

Figure 3. The upper panel is the merged light curve of the photometric V band and spectroscopic f_{5100} in units of 10^{-15} erg cm^{-2} s^{-1} Å^{-1}, and the lower panel is the Hα emission-line light curve in units of 10^{-14} erg cm^{-2} s^{-1}, obtained from spectroscopic data after smoothing by five consecutive data points.

Table 2
Light-curve Table

Time_MJD (1)	c_flux (2)	c_error (3)	l_flux (4)	l_error (5)	Type (6)
59648.953264	2.8425	0.0217	⋯	⋯	P
59648.964006	2.8587	0.0091	34.9334	0.7723	S
59648.967928	2.8765	0.0220	⋯	⋯	P
59648.982326	2.8850	0.0226	⋯	⋯	P
59648.984049	2.8886	0.0093	33.8328	0.6847	S
59648.989542	2.8823	0.0091	33.4908	0.6045	S

Note. Column (1): Modified Julian Date (Time_MJD). Columns (2) and (3): the merged continuum flux and error for the photometric V band (denoted as P) and spectroscopic f_{5100} (denoted as S), measured in units of 10^{-15} erg cm^{-2} s^{-1} Å^{-1}. Columns (4) and (5): the Hα line flux and its error, also in units of 10^{-15} erg cm^{-2} s^{-1}. Column (6): the type of continuum flux, where P indicates photometric V-band flux and S denotes spectroscopic flux measured at 5100 Å. The complete table is available in a machine-readable format, with a portion provided here for reference.

(This table is available in its entirety in machine-readable form in the online article.)

Table 3
Light-curve Variability Statistics

DAY (1)	Light Curve (2)	Median (3)	R_{max} (4)	F_{var} (%) (5)
10th Mar	$F_{5100}+V$ band	28.97 ± 0.12	1.12 ± 0.01	2.60 ± 0.24
	Hα	331.20 ± 2.80	1.18 ± 0.04	3.67 ± 0.54
11th Mar	$F_{5100}+V$ band	26.90 ± 0.27	1.28 ± 0.02	6.89 ± 0.58
	Hα	299.73 ± 1.85	1.15 ± 0.03	2.70 ± 0.43
10th +11th Mar	$F_{5100}+V$ band	28.56 ± 0.19	1.30 ± 0.02	6.38 ± 0.40
	Hα	314.45 ± 2.81	1.33 ± 0.04	6.31 ± 0.53

Note. Column (1): day. Column (2): nature of the light curve. Column (3): median flux of the light curve in units of 10^{-15} erg s^{-1} cm^{-2} Å^{-1} for f_{5100} and units of 10^{-15} erg s^{-1} cm^{-2} for emission lines. Column (4): the ratio of the maximum to minimum flux variation. Column (5): fractional rms variability in percentage.

Additionally, the ratio of maximum to minimum flux variation (R_{max}) is calculated for these light curves. Table 3 shows variability statistics including the median flux, F_{var}, and R_{max} for March 10, March 11, and the entire light curve. The variability and R_{max} are similar to the range found in H. Cho et al. (2020). The R_{max} ranges from 1.18 to 1.33 for the Hα emission line and from 1.12 to 1.30 for the merged continuum light curve.

3.2. Time-lag Analysis

Technical issues resulted in interruptions to continuous observations, leading to gaps in the spectroscopic light curve on both nights, as is evident in Figure 3. Consequently, the light curve is divided into four segments (two for each day) before being used to measure the lag. Specifically, for March 10, only the second part of the light curve is used, as the first part lacked sufficient data points and monitoring duration.

3.2.1. Interpolated Cross-correlation Function and JAVELIN

The lag between the continuum and Hα emission line is measured using two methods, namely the interpolated cross-correlation function (ICCF; B. M. Peterson et al. 1998)[12] and JAVELIN (Y. Zu et al. 2011, 2013).[13] These methods are widely used (see; B. M. Peterson et al. 1998, 2004; M. C. Bentz et al. 2014; A. J. Barth et al. 2015; J.-H. Woo et al. 2024, and references therein) with consistent results (R. Edelson et al. 2019). In ICCF, the nature of the correlation between the two data sets is identified through cross-correlation. The lag between the optical continuum and Hα emission-line flux is

---

[12] https://bitbucket.org/cgrier/python_ccf_code/src/master/
[13] https://github.com/nye17/JAVELIN

Table 4
Lag Table

DAY		ICCF		JAVELIN	PyI^{2}CCF	
Date (1)	Segment (2)	Lag (3)	r_{max} (4)	Lag (5)	Lag (6)	p-value (7)
March 10	Entire[a]	$267.3^{+9.2}_{-16.7}$	0.70	$268.4^{+14.6}_{-302.8}$	$268.0^{+8.0}_{-10.2}$	0.31
	Part 2*	$84.5^{+11.4}_{-126.6}$	0.45	$86.1^{+7.6}_{-125.3}$	$86.5^{+7.5}_{-130.0}$	0.60
March 11	Entire	$150.5^{+25.8}_{-23.7}$	0.78	$185.3^{+9.7}_{-9.3}$	$148.5^{+26.4}_{-24.6}$	0.35
	Part 1	$103.1^{+17.4}_{-13.3}$	0.60	$92.6^{+10.3}_{-57.4}$	$101.1^{+15.4}_{-12.5}$	0.87
	Part 2	$124.2^{+6.6}_{-8.6}$	0.90	$[122.3^{+9}_{-4}]$[b]	$125.0^{+6.2}_{-6.1}$	0.04
March 10+March 11	Entire*	$205.6^{+16.6}_{-11.1}$	0.38	$205.0^{+5.5}_{-4.4}$	$205.0^{+17.0}_{-9.3}$	0.54

Note. Lag in the rest frame between the combined continuum (V band and f_{5100}) versus Hα light curves obtained using ICCF, JAVELIN, and PyI^{2}CCF for different days and segments. Column (1): date of observation. Column (2): segment of the light curve. Column (3): ICCF lag in minutes. Column (4): cross-correlation coefficient r_{max}. Column (5): JAVELIN lag in minutes. Column (6): PyI^{2}CCF lag in minutes. Column (7): PyI^{2}CCF null hypothesis value (p).
[a] Detrended light curves.
[b] Considered a second peak for lag estimation.

determined with a lag limit of −60 to 160 minutes for segments and −60 to 300 minutes for entire light curves. In ICCF, one light curve is linearly interpolated while keeping the other light curve fixed, and vice versa. Subsequently, the average of the two CCFs yields the final ICCF.

The Monte Carlo method of flux randomization and random subset selection is used to measure the uncertainty in the lag (B. M. Peterson et al. 1998, 2004), with a median of the centroid (τ_{cent}; covering $0.8 \times r_{max}$, where r_{max} is the maximum correlation coefficient achieved) distribution as the lag. Table 4 depicts the lag results with different methods of lag estimation.

JAVELIN was developed by Y. Zu et al. (2011, 2013) to model the driving light curve with a DRW model. This DRW-modeled light curve utilizes the transfer function to derive the other related light curves, typically employing a top-hat function as the transfer function. Error estimation employs the Markov Chain Monte Carlo methodology to compute statistical confidence limits for each best-fit parameter. This approach simultaneously enables continuum and emission-line light-curve modeling. The DRW process (B. C. Kelly et al. 2009, 2014) accurately predicts the nature of continuum variations in AGNs for long, short, and even multiband light curves, with some tenable deviations as seen (e.g., I. M. McHardy et al. 2006; R. F. Mushotzky et al. 2011). Smaller uncertainties in lag estimation are provided by JAVELIN compared to the ICCF method (see C. J. Grier et al. 2017; R. Edelson et al. 2019; Z. Yu et al. 2020). However, they might be more affected by seasonal gaps that could infer a negative false rate (for more details, see J.-H. Woo et al. 2024).

The results of the time-series analysis are plotted in Figure 4, where the upper-left panel displays a segment of the continuum light curve, while the lower-left panel shows a segment of the emission-line light curve. The lag is measured for various segments of the emission-line light curve concerning the entire continuum light curve for the respective days. The lag results were considered reliable when the ICCF correlation coefficient (r_{max}) was more than 0.5 (as shown in Figure 4). For a lag limit of −60 to 160 minutes, a lag of approximately 86 minutes is obtained for the second part of March 10 with JAVELIN, consistent with the ICCF method, which provided a lag of 85 minutes. The entire light curve of the same day peaked at 268 minutes, with a lag limit of −60 to 300 minutes. The more considerable uncertainty in these cases is due to detecting two peaks in the lag distribution. On the following day, March 11,

with the same lag limit of −60 to 160 minutes, the lag for the first segment was 93 and 103 minutes with JAVELIN and ICCF, respectively.

For the second segment of March 11, the result from the ICCF is 124 minutes. However, JAVELIN evidences two peaks in the lag distribution, which are around 0 and 122 minutes. The more substantial first peak leads to a lag of ∼3 minutes, with considerable uncertainty. However, if we remove the first peak around 0 minutes, it is evident that the lag result for 0 to 160 minutes matches with the ICCF lag stated in Table 4. The entire light curve for March 11 shows slightly different results using both methods, with a lag limit of −60 to 300 minutes as 185 minutes with JAVELIN and 150 minutes with ICCF. The lag is also calculated by combining both days' light curves, shown in the Table 4 for the limit −60 to 300 minutes. A lower cross-correlation coefficient r_{max} is encountered due to noise and gaps in the light curve. The results for a few chunks of the light curve are obtained with detrending, discussed in Section 3.2.2.

3.2.2. Detrending the Light Curve

Understanding the short-term intrinsic behavior is crucial for understanding the variability and estimating a reliable lag. However, long-term trends, resulting, for example, from red-noise leakage (W. F. Welsh 1999), pose a challenge when analyzing short-term behavior and can introduce bias into cross-correlation lag results. An effective approach is to eliminate these long-term trends, which not only aids in understanding short-term variability, but also improves lag estimation (see Z.-X. Zhang et al. 2019; J.-H. Woo et al. 2024). To achieve this, we fit a straight line to each light curve and subtract it from the original, removing the trend. Subsequently, we cross-correlate the continuum and line light curves to measure the lag between them. It is worth noting that higher-order polynomials can introduce unnatural or false signals and patterns into the light curve, potentially impacting lag estimates.

In some parts of the light curves, two prominent peaks conflicted with the lag estimation through ICCF and JAVELIN. Consequently, we detrended the March 10 light curve (entire and in parts), which improved the cross-correlation coefficient (r_{max}). In Figure 4, the detrended light curves are shown for the March 10 second part and the entire light curves of the continuum and Hα emission line. Similarly, the lag calculation for the entire two days is significantly affected by detrending and results in one peak of
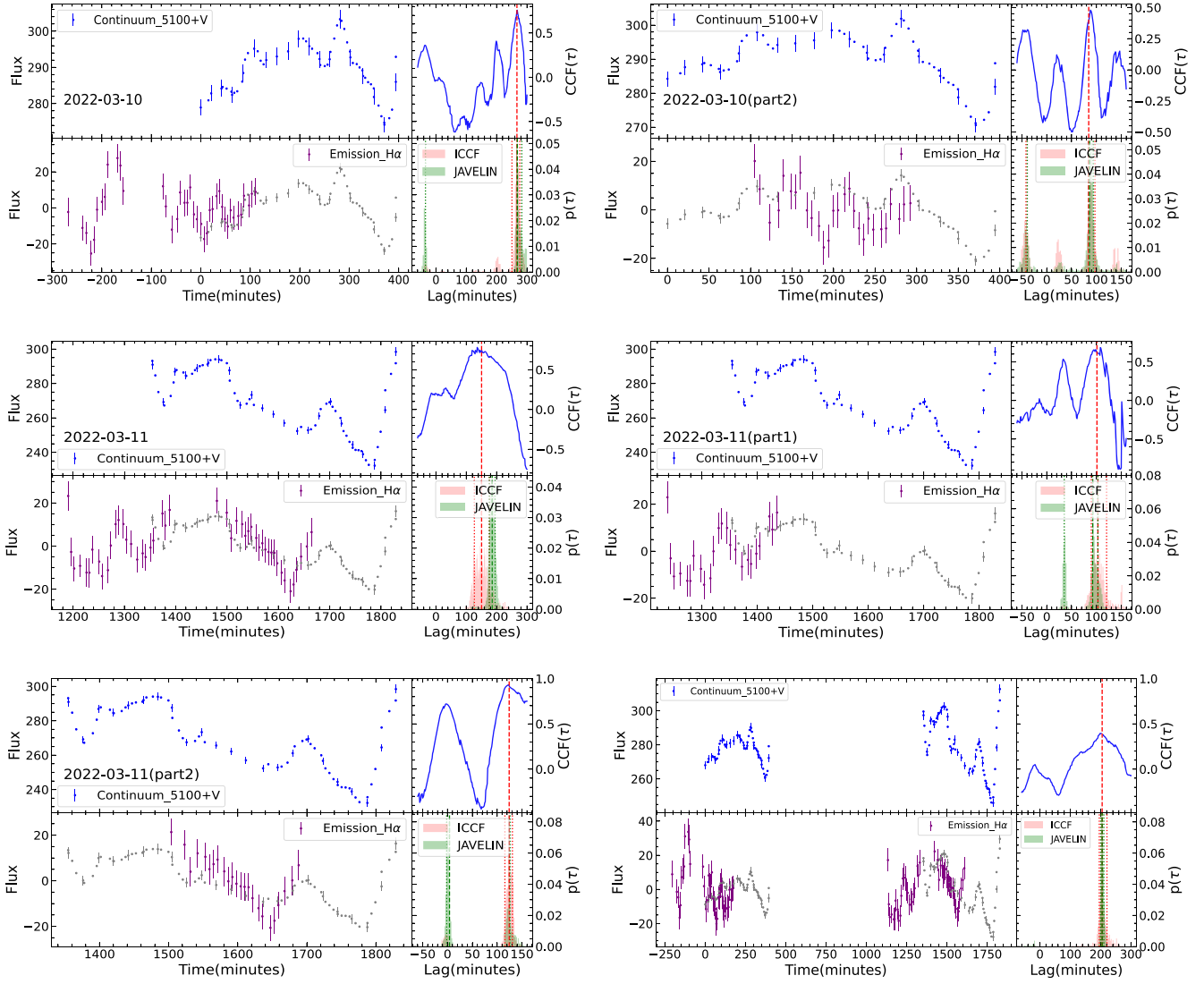
Figure 4. The lag results are plotted; the upper-left panel shows the merged V-band and continuum flux at 5100 Å in units of 10^{-17} erg cm^{-2} s^{-1} Å^{-1}, and the lower-left panel shows the emission-line light curve in units of 10^{-17} erg cm^{-2} s^{-1}. The mean-subtracted light curves shown are matched by normalizing the continuum light curve and shifting the emission-line light curve to the final adopted lag values mentioned in Table 4. The upper-right panel depicts the ICCF coefficient (r) resulting from the continuum and emission-line light curve with respect to the lag in minutes. The lower-right panels show the lag histograms obtained using the ICCF and JAVELIN methods. Here, subplots 1, 2, and 6 show the detrended light curves and their respective detrended lag results.

around 205 minutes, shown in Section 5. However, for the March 11 second part, the detrending does not pose any difference in the results, especially with JAVELIN.

3.2.3. Simulations

The publicly available PyI²CCF code developed by H. Guo et al. (2022) is used,[14] implementing the method described in V. U et al. (2022). This method assesses the significance of lag measurements or verifies the reliability of the ICCF method. It is grounded on the null hypothesis, which posits that when two random uncorrelated light curves are cross-correlated, the resulting r_{max} should be greater than or equal to the observed cross-correlation ($r_{max,obs}$) obtained from real light curves. Mock light curves are generated by the code based on the DRW model with the same noise and cadence as the actual light curves (see also S. Pandey et al. 2022; V. U et al. 2022; D. H. Gonzalez-Buitrago et al. 2023; J.-H. Woo et al. 2024).

Specifically, 1000 mock light curves are generated for the continuum and Hα emission-line light curves. The lag values in minutes alongside the null hypothesis value (p) are presented in the last column of Table 4. Certain light-curve parts in Table 4 exhibit more noise and, consequently, poorer quality, as reflected in the higher p-value. Applying the criteria for lag reliability $p \leqslant 0.2$ (H. Guo et al. 2022; V. U et al. 2022; J.-H. Woo et al. 2024) and $r_{max} > 0.5$, we identified the second segment of March 11 as providing the most reliable lag, which is $125.0^{+6.2}_{-6.1}$ minutes, and we used it for the black hole mass measurement. We caution that the above may not be the best criteria for lag reliability.

3.3. Line Width and Black Hole Mass Measurement

To construct the mean spectrum, we first aligned all spectra to match the resolution of the Hα emission line using mapspec (M. M. Fausnaugh 2017).[15] Consequently, the mean

---

[14] https://github.com/legolason/PyIICCF/

[15] https://github.com/mmfausnaugh/mapspec

spectrum is constructed for each part of the observations using the following approach:

$$F(\lambda) = \frac{1}{N} \sum_{i=0}^{N-1} F_i(\lambda),$$ (2)

where $F_i(\lambda)$ is the ith spectrum of the N spectra that comprise the database. For March 10, we acquired 40 spectra, with 28 available in the second segment. Similarly, for March 11, 24 spectra were obtained for each segment, resulting in 48 spectra for the entire night. Figure 2 displays one such mean spectrum obtained from March 11.

As mentioned in Section 2.2.3, the mean spectrum is also decomposed into broad and narrow components of the Hα line. Then the best-fit broad Hα component is used to measure the FWHM and σ_{line} in the wavelength region of 6500–6600 Å.

Following B. M. Peterson et al. (2004), the FWHM is calculated by finding half-maximum from both the left (λ_{left}) and right (λ_{right}) sides of the curve. Eventually, the FWHM is the $\lambda_{\text{right}} - \lambda_{\text{left}}$ wavelengths, whereas for the calculation of the σ_{line}, the flux-weighted line center is first determined as follows:

$$\lambda_0 = \frac{\int \lambda f_\lambda \, d\lambda}{\int f_\lambda \, d\lambda},$$ (3)

and the line dispersion as follows:

$$\sigma_{\text{line}}^2 = \frac{\int \lambda^2 f_\lambda \, d\lambda}{\int f_\lambda \, d\lambda} - \lambda_0^2.$$ (4)

The FWHM and σ_{line} are measured using the Monte Carlo bootstrap technique (B. M. Peterson et al. 2004), where 5000 realizations are run to measure them after N spectra were chosen from the pool of N spectra. The endpoints of the Hα region (6500–6600 Å) are randomly adjusted within a range of ±10 Å from the initially selected values. The distribution for the FWHM and σ_{line} is obtained after running 5000 realizations, estimating the uncertainties in the line width and black hole mass measurement. The FWHM and σ_{line}, along with their measured uncertainties (the 16th and the 84th percentiles of the distribution), are presented. Finally, the FWHM and σ_{line} are corrected with the instrumental resolution.

Given that the gravitational potential of the black hole influences the movement of gas within the BLR, the mass of the black hole can be measured by multiplying the size of the BLR (R_{BLR}) and the velocity width of the broad emission lines (ΔV) using the virial relation:

$$M_{\text{BH}} = \frac{f \times R_{\text{BLR}}(\Delta V)^2}{G},$$ (5)

where f is a dimensionless scale factor that depends on the kinematics and geometry of BLR gas clouds. The BLR size is directly measured with lag(τ) in minutes using $R_{\text{BLR}} = c\tau$ from Table 4, with c as the speed of light.

The scale factor (f) is taken from J. H. Woo et al. (2015), which is 1.12 and 4.47 when the line width is chosen as the FWHM and σ_{line}, respectively. The resolution-corrected σ_{line} and FWHM from the mean spectrum are measured to be $544.7^{+22.4}_{-25.1}$ km s^{-1} and $810.2^{+86.8}_{-91.8}$ km s^{-1}, respectively. Combining the PyI^{2}CCF lag of 125 minutes (March 11, second part)

with the σ_{line} and FWHM, the black hole mass is calculated to be $2.2^{+0.2}_{-0.2} \times 10^4 M_\odot$ and $1.2^{+0.3}_{-0.2} \times 10^4 M_\odot$, respectively.

Since the σ_{line} is less sensitive to the peak and provides a more accurate black hole mass measurement than the FWHM (e.g., B. M. Peterson et al. 2004; B. M. Peterson 2014), a black hole mass of $2.2^{+0.2}_{-0.2} \times 10^4 M_\odot$ is found for NGC 4395 as the best measurement.

4. Discussion

4.1. Previous Studies

An extensive range of black hole masses for NGC 4395 have been reported in the literature, e.g., the mass of the black hole was calculated to be $1.2 \times 10^5 M_\odot$ by S. B. Kraemer et al. (1999), using photoionization modeling with an FWHM of Hβ as 1500 km s^{-1}, while A. V. Filippenko & L. C. Ho (2003) provided a mass range of $250 M_\odot \leqslant M_{\text{BH}} \leqslant 6 \times 10^6 M_\odot$, based on the Eddington limit and dynamics of the stellar cluster. Utilizing X-ray, UV, and optical photometric data points along with spectroscopic observations, L.-B. Desroches et al. (2006) confirmed the reprocessing model and measured a black hole mass of $3 \times 10^5 M_\odot$ using He II, Hα, Hβ, and Hγ emission lines. The gas dynamics of the central region for NGC 4395 have been studied by a few authors, such as M. d. Brok et al. (2015) and C. Brum et al. (2019), to estimate the $\sigma_\star$, which can help constrain the black hole mass. Unfortunately, the disk continuum emission might have been dominated by the CO absorption band head, which makes it insignificant and prevents the measurement of the stellar dispersion velocity. With single-epoch spectroscopic data obtained using Gemini GMOS-IFU, the black hole mass of NGC 4395 was found to be $2.5 \times 10^5 M_\odot$, with the Hα FWHM being 785 km s^{-1} using a nuclear spectrum (C. Brum et al. 2019). The Gemini NIFS spectrum was used by M. d. Brok et al. (2015) to measure the best-fit black hole mass of $4^{+8}_{-3} \times 10^5 M_\odot$ (3σ uncertainties), with combined modeling of the stellar populations of the nuclear star cluster (NSC) and the dynamics of the molecular gas.

Several attempts at RM have been made for NGC 4395. For example, B. M. Peterson et al. (2005) performed RM using the C IV $\lambda1549$ emission line, providing a BLR size of 48–66 light minutes. Combining the lag with an FWHM ($\sim\sigma_{\text{line}}$) of ~3000 km s^{-1} from the rms spectra, they measured a black hole mass of $3.6 \pm 1.1 \times 10^5 M_\odot$. It is important to mention that the C IV line depicted in B. M. Peterson et al. (2005) exhibits an irregular line profile, coupled with a noisy rms spectrum, which could potentially hinder its accurate measurement (as discussed in H. Cho et al. 2021). The first reliable black hole mass was reported by J.-H. Woo et al. (2019), who determined an ~80 minutes lag based on narrowband photometry RM results and measured the σ_{line} of Hα as 426 ± 2.5 km s^{-1} from the mean spectrum, obtaining the black hole mass as $\sim10,000 M_\odot$. However, as mentioned in Section 1, the continuum contribution in the narrowband Hα filter can be a dominant source of uncertainty in the lag measurement. J.-H. Woo et al. (2019) assumed the variability of continuum in the Hα band (6450–6650 Å) is similar to what they measured in the photometric continuum V band (4800–6500 Å). Further, they convolved the transmission curve of the MDM Hα filter with the mean GMOS spectrum and calculated a mean continuum contribution of 18.3%. The continuum fraction in each Hα epoch was estimated by scaling the V-band variability by a factor of 0.183, subtracted from each Hα epoch. It is worth noting that this

represents the maximum calculated continuum contribution, as the continuum variability in the Hα filter is expected to be no greater than that in the V-band filter. H. Cho et al. (2020) varied the scaling parameter by assuming the continuum inside the Hα filter has a similar variability behavior to the photometric continuum V band. The variability is varied with a range of 0%–100% to that of the Hα emission-line flux, using the variability amplitude parameter equation presented in their Section 3.3.1. However, their PRM analysis is affected by baseline mismatches between Hα and V-band observations, weak variability, and significant uncertainty in Hα photometry, all impacting lag measurement. By decomposing and separating the emission lines with the continuum using flux-calibrated spectra, the spectroscopic RM can accurately predict the variability and contribution of the continuum and further the lag measurement.

This black hole mass was updated as $1.7 \pm 0.3 \times 10^4 M_\odot$ by H. Cho et al. (2021), as the σ_{line} of Hα was remeasured as $586 \pm 19 \, \text{km s}^{-1}$, based on a higher-quality spectrum by fitting the broad component with a double Gaussian. H. Cho et al. (2021) attempted spectroscopic RM of NGC 4395. However, they could not obtain a reliable lag measurement due to bad weather losses and insignificant detection of variability structure in the light curve. At the same time, they constrained the upper limit of the reverberation black hole mass as $4 \times 10^4 M_\odot$, with the lag as less than 3 hr. Recently, H. Gu et al. (2024) employed broadband PRM by analyzing the g- and r-band data of NGC 4395 from recent studies (J. W. Montano et al. 2022; I. M. McHardy et al. 2023), measuring an Hα lag of 40–90 minutes. We performed spectroscopic RM and performed detailed spectral decomposition to construct the emission-line light curve. These good-quality light curves allowed us to successfully estimate a BLR size of 125 light minutes using both ICCF and JAVELIN. Moreover, we measured the velocity dispersion and constrained the black hole mass to be $2.2^{+0.2}_{-0.2} \times 10^4 M_\odot$, which is consistent with the findings of J.-H. Woo et al. (2019), H. Cho et al. (2020), and H. Cho et al. (2021).

The FWHM for Hα was used as $1500 \pm 500 \, \text{km s}^{-1}$ (lag ∼3.6 hr) by H. Edri et al. (2012), resulting in a black hole mass estimation, i.e., $4.9 \pm 2.6 \times 10^4 M_\odot$. They further argued that FWHM provides a better measurement for line width than taking the second moment, i.e., σ_{line}, because the broad lines become narrower, so a single-Gaussian fit might not suit it. Instead, modeling the broad component with a Lorentzian might be more appropriate (W. Kollatschny & M. Zetzl 2011). However, H. Cho et al. (2021) and J.-H. Woo et al. (2019) suggested that Hα fits very well with a double-Gaussian model. It should be noted that this study has used a double Gaussian to model the broad Hα line, similar to modeling with a Lorentzian profile.

The rms spectrum of NGC 4395 was used by B. M. Peterson et al. (2005) and L.-B. Desroches et al. (2006) to measure the line width and calculate the black hole mass. On the other hand, it was noted by J.-H. Woo et al. (2019) that the σ_{line} is approximately similar when using both the rms and mean spectra. In our study, the rms spectrum was noisy and, consequently, the FWHM and σ_{line} were obtained from the mean spectrum. Our results are slightly lower than previous estimates, with the FWHM measured at $810.2^{+86.8}_{-91.8} \, \text{km s}^{-1}$ and the σ_{line} at $544.7^{+22.4}_{-25.1} \, \text{km s}^{-1}$ for the second part of the observations on March 11. Furthermore, our Hα line width, denoted as σ_{line}, is 7% narrower compared to the Hα line profile presented by H. Cho et al. (2021), which was modeled

using two broad components. Conversely, it is 28% wider than the σ_{line} value of $426 \, \text{km s}^{-1}$ reported by J.-H. Woo et al. (2019), derived from a single-Gaussian model.

The choice of the scale factor (f) value can significantly affect the mass measurement. The f value of 5.5 adopted by B. M. Peterson et al. (2005) was determined empirically by C. A. Onken et al. (2004), with σ_{line} as the line-width estimator. This value of f was derived under the assumption that the relationship between the central black hole mass and $\sigma_\star$, the M_{BH}–$\sigma_\star$ relation, is the same for both quiescent and active galaxies. A much smaller value was chosen by H. Edri et al. (2012), as 0.75 with FWHM as the line width, based on the assumption of simple Keplerian motion, resulting in a smaller measured black hole mass. Similar to C. A. Onken et al. (2004), J. H. Woo et al. (2015) added a large number of sources having RM-based masses to the M_{BH}–$\sigma_\star$ relation and found the f to be 1.12 and 4.47 with the FWHM and σ_{line} as the line width values, respectively. Hence, we have used $f = 4.47$ (J. H. Woo et al. 2015) with σ_{line} to calculate the black hole mass of NGC 4395. Dynamical modeling of RM data could help to better measure the f value for NGC 4395.

4.2. Host Galaxy Contribution

The host galaxy and an NSC contribute to the measured luminosity. The host galaxy contribution (including the study of NSCs) has been separated from the AGN core by previous authors (A. V. Filippenko & L. C. Ho 2003; D. T. Cameron et al. 2012) using the GALFIT software (C. Y. Peng et al. 2002, 2010) or employing different models (H. Cho et al. 2020). The GALFIT software is used to fit the galaxy profile by modeling it. An 18″ by 15″ rectangle was used by D. T. Cameron et al. (2012) to fit the central engine of NGC 4395 with three profile model components: a nuclear point source, a Sérsic component, and an exponential disk. The Sérsic component models the NSC; the bright irregular features and Galactic stars were masked during fitting. The nuclear point source was subtracted, and the nonnuclear flux density in the u, v, and b bands was estimated. Additionally, two profile model components were used by H. Cho et al. (2020), a point source and an exponential disk, estimating the host galaxy contribution to the total flux at 16%.

The mean spectrum of the second segment of the March 11 light curve was used, as well as the monochromatic luminosity at 5100 Å, i.e., λL_λ measured as $2.87 \pm 0.01 \times 10^{40} \, \text{erg s}^{-1}$. Image decomposition using GALFIT on the mean V-band images was performed. The model components used are a PSF to model the AGN core within 8″ and an exponential disk with the addition of the Sérsic profile for the host galaxy modeling. We found a host contribution of 22.6%, slightly larger than the values reported by H. Cho et al. (2020). Considering the NSC flux of $\lambda L_{\lambda;\text{NSC}} = 3.59 \times 10^{39} \, \text{erg s}^{-1}$ from the stellar cluster (D. J. Carson et al. 2015), we measured the host and NSC-subtracted final λL_{5100} to be $1.86 \pm 0.01 \times 10^{40} \, \text{erg s}^{-1}$.

4.3. Radius–Luminosity Relation

To compare NGC 4395 with other RM sources, it has been plotted in the well-known Hβ BLR size versus optical luminosity at 5100 Å established for AGNs. The measured Hα lag ($\tau_{\text{H}\alpha}$) has been converted to Hβ lag ($\tau_{\text{H}\beta}$) using $\tau_{\text{H}\alpha} : \tau_{\text{H}\beta} = 1.68 : 1$ provided by H. Cho et al. (2023). The measured Hβ lag of 74.8 minutes is plotted against L_{5100} of $1.86 \pm 0.01 \times 10^{40} \, \text{erg s}^{-1}$ in Figure 5. Similar to H. Cho et al.
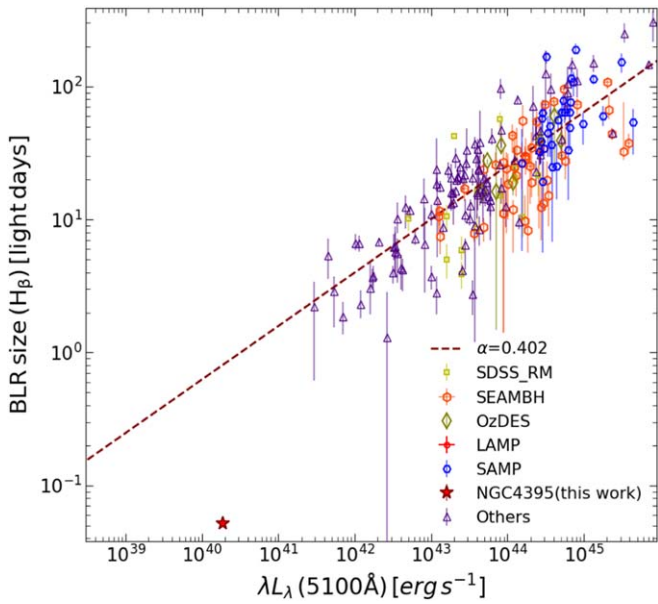
Figure 5. The plot depicts the Hβ BLR size vs. optical luminosity at 5100 Å. NGC 4395 lies at the low-luminosity end, with an Hβ BLR size of 74.8 light minutes. The other RM sources, such as SEAMBHs (P. Du et al. 2016, 2018; C. Hu et al. 2021; S.-S. Li et al. 2021; orange open circles), SDSS-RM (C. J. Grier et al. 2017; yellow open squares), OzDES (U. Malik et al. 2023; green open diamonds), LAMP (V. U et al. 2022; red open circles), SAMP (J.-H. Woo et al. 2024; blue open hexagons), and others (including, M. C. Bentz et al. 2013; S. Park et al. 2017; S. Rakshit et al. 2019; E. D. Bontà et al. 2020; S. Rakshit 2020; S. Pandey et al. 2022; purple open triangles) are shown. The brown dashed line shows the best-fit R–L relation as obtained by J.-H. Woo et al. (2024).

(2020), NGC 4395 has been found to have a small offset from the fitted slope in the R_{BLR}–L relation. The reasons for such deviation could be partly due to either the uncertainty in the AGN luminosity measurement or, intrinsically, the R_{BLR}–L relation for typical broad-line AGNs not being valid for low-luminosity objects. Indeed, the measured luminosity is in the upper range compared to previous works. For example, an L_{5100} of 5.9×10^{39} erg s^{-1} was found by B. M. Peterson et al. (2005), while H. Cho et al. (2020) calculated it to be 8.52×10^{39} erg s^{-1}, and 6.6×10^{39} erg s^{-1} was measured by A. V. Filippenko & L. C. Ho (2003).

The uncertainty could also arise from the choice of plotting the Hα line lag, whereas the BLR size and luminosity relation are based on the Hβ line lag. Recently, a best-fit size–luminosity relation, including NGC 4395, was obtained by H. Cho et al. (2023), as shown in Figure 6. According to this, the expected Hα lag for NGC 4395 is 374 minutes for our measured L_{5100}, i.e., a factor of ~3 times larger than our estimated lag of 125 minutes. With the Greene & Ho + Bentz (GH+B) relation mentioned in H. Cho et al. (2023), the $\tau_{H\alpha}$ is estimated as 252 minutes, with $L_{H\alpha}$ as 6.64×10^{37} erg s^{-1}. Both of these estimates are approximately similar and more than twice longer than our measurement for $\tau_{H\alpha}$. This agrees with H. Cho et al. (2023) that the GH+B relation provides lag results overestimated by 2 times for IMBHs or low-luminosity AGNs with $L_{H\alpha} < 10^{42}$ erg s^{-1}. This can further overestimate black hole masses by 2–3 times for IMBHs. X.-G. Zhang et al. (2007) noted that low-luminosity AGNs, characterized by $L_{H\alpha} < 10^{41}$ erg s^{-1}, exhibit a lower ionization parameter and lower electron density in the BLR, potentially leading to deviations from the R_{BLR}–L relation. However, it was also mentioned that NGC 4395 could compensate for the deviation with a high accretion rate and might be consistent with the
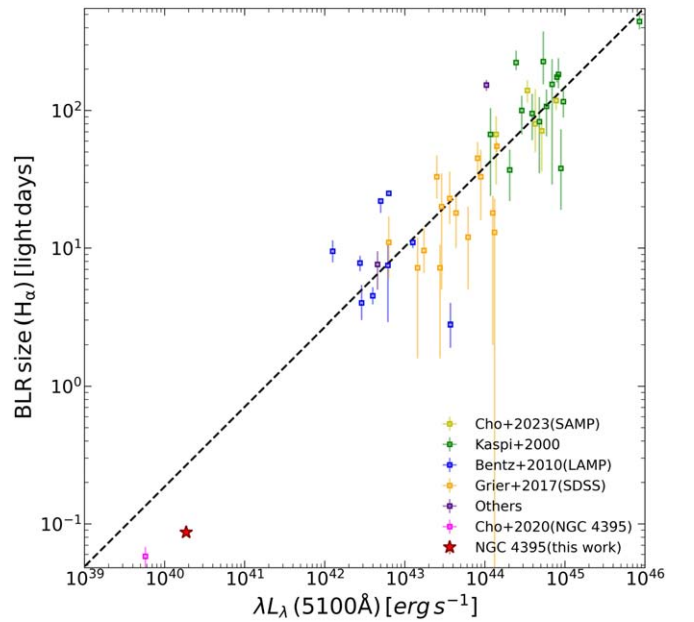

Figure 6. The Hα BLR size vs. monochromatic continuum luminosity at 5100 Å is plotted. Various Hα RM sources (S. Kaspi et al. 2000; M. C. Bentz et al. 2010; C. J. Grier et al. 2017; H. Cho et al. 2020; J.-H. Woo et al. 2024), along with others (such as S. G. Sergeev et al. 2016; H.-C. Feng et al. 2021; S.-S. Li et al. 2022), and the best-fit relation from H. Cho et al. (2023), are plotted. The source NGC 4395 is plotted with our best measurement of 125 light minutes in comparison to the 84 minutes lag obtained by H. Cho et al. (2020).

R_{BLR}–L relation. However, the accretion rate of NGC 4395 is measured to be smaller, ~0.06. It was stated by L. Pei et al. (2017) that low-accretion-rate sources such as NGC 5548 can deviate from R_{BLR}–L, which could support the small deviation of NGC 4395. Estimations of RM masses of more low-luminous sources are needed to address the issue.

4.4. Black Hole Mass–Stellar Velocity Dispersion

Previous studies (J. Kormendy & L. C. Ho 2013; J.-H. Woo et al. 2013, 2015) have concluded that the AGNs preserve the same correlation between black hole mass (M_{BH}) with its $\sigma_\star$ as confirmed for inactive galaxies. Hence, can the same correlation be trusted for low-luminous IMBHs? Exploring the lower-mass range is crucial to understanding how black holes affect their host galaxy growth and evolution.

An attempt was made by M. d. Brok et al. (2015) to measure the $\sigma_\star$ of the NSC to constrain the central black hole mass in the NGC 4395 galaxy. Dynamical modeling of molecular hydrogen (H$_2$) gas was employed through imaging and spectroscopy using the Hubble Space Telescope/Wide Field Camera 3 and Keck II telescope, respectively. Unfortunately, a reliable $\sigma_\star$ could not be obtained, due to the absence of CO absorption band heads, typical of evolved stellar populations in nearby galaxies. An upper limit of the velocity dispersion <30 km s^{-1} (as predicted by A. V. Filippenko & L. C. Ho 2003) was provided against their unreliable estimation below 15 km s^{-1}. Similarly, C. Brum et al. (2019) found the $\sigma_\star$ of ionized gases such as Paβ, Hα, and [N II] to be around 60 km s^{-1} to the east and 40 km s^{-1} to the west, with respect to the nucleus of NGC 4395. However, the molecular hydrogen H$_2$ had σ_{line} ~30 km s^{-1}, similar to what A. V. Filippenko & L. C. Ho (2003) obtained for stellar dispersion velocity ($\sigma_\star$) using Ca II absorption features. The upper limit for $\sigma_\star$ was set to be 30 km s^{-1} (see A. V. Filippenko & L. C. Ho 2003) using Ca II absorption features.

Due to the challenges encountered in previous attempts to measure $\sigma_\star$ by previous authors (see M. d. Brok et al. 2015; C. Brum et al. 2019), the dispersion of narrow emission lines is used as a substitute for $\sigma_\star$. R. O. Sexton et al. (2021) and H. A. N. Le et al. (2023) argued that the narrow line [O III] $\lambda5007$ of AGNs is highly correlated with $\sigma_\star$ and hence can be used as a substitute for it. Hence, we measured $\sigma_{[O\,III]\lambda5007}$, which was found to be 91.3 ± 5.8 km s^{-1} after correcting the instrumental resolution. Additionally, the best-fit single-Gaussian modeling of the [S II] line provided a width of 70 ± 3.8 km s^{-1}.

Sources consisting of the mass of inactive galaxies measured using dynamical modeling (J. Kormendy & L. C. Ho 2013) and RM AGNs, compiled by J. H. Woo et al. (2015), are shown in Figure 7, along with the best-fit relation taken from J. Kormendy & L. C. Ho (2013) and J. H. Woo et al. (2015). NGC 4395 is placed with previous and current estimates of $\sigma_\star$ with our measured black hole mass, i.e., $2.2^{+0.2}_{-0.2} \times 10^4 M_\odot$. The source closely follows the $M_{BH}-\sigma_*$ relation if $\sigma_* = 30$ km s^{-1} is used; however, it shows significant offsets when $\sigma_{[O\,III]\lambda5007}$ is used as a surrogate of $\sigma_\star$. We note that J.-H. Woo et al. (2019) found their [S II] doublets to be better fitted with double-Gaussian models for each line, one for core and another for the wing, with values $\sigma_{core} = 18 \pm 1$ km s^{-1} and $\sigma_{wing} = 100 \pm 5$ km s^{-1}. However, a single Gaussian was enough to model the [S II] line in our case. Consequently, considering the upper limit of the stellar dispersion velocity of 30 km s^{-1} (A. V. Filippenko & L. C. Ho 2003), J.-H. Woo et al. (2019) used their measured σ_{core} component in their analysis.

5. Conclusions

Photometric and spectroscopic monitoring were performed for NGC 4395 to measure the BLR size and black hole mass. The main conclusions are as follows:

1. The fractional variability for merged V-band and spectroscopic optical continuum flux for March 10 is 2.6%, for March 11 is 7%, and for the entire light curve including both days is 6%, with R_{max} ranging between 1.12–1.30. For the Hα light curve, the F_{var} is maximum at 6.3% for the entire light curve, with R_{max} as 1.33.
2. The measured Hα BLR size is $125.0^{+6.2}_{-6.1}$ light minutes. This is the best measurement using the second part of the March 11 light curve.
3. The line width, FWHM, and σ_{line} are measured from the mean spectrum constructed from the March 11 second part, consisting of a total of 24 spectra. The σ_{line} is calculated to be $544.7^{+22.4}_{-25.1}$ km s^{-1} and the FWHM as $810.2^{+86.8}_{-91.8}$ km s^{-1}.
4. The σ_{line} is used to calculate the black hole mass, which is found to be $2.2^{+0.2}_{-0.2} \times 10^4 M_\odot$, which lies within the range of masses provided in the literature.
5. The bolometric luminosity (L_{BOL}) is measured as 1.67×10^{41} erg s^{-1} and the Eddington ratio (λ_{EDD}) is 0.06.
6. NGC 4395 is placed in the $R_{BLR}-L$ relation for SMBHs, where the source shows a 3 times smaller BLR size than expected. RM studies of more such low-luminous AGNs will allow us to calibrate a better $R_{BLR}-L$ relation.
7. Considering the lower limit of $\sigma_\star = 30$ km s^{-1} as provided by the literature, the source closely follows the $M_{BH}-\sigma_\star$ relation; however, it shows significant deviation when [O III]$\lambda5007$ is used as a proxy of $\sigma_\star$.
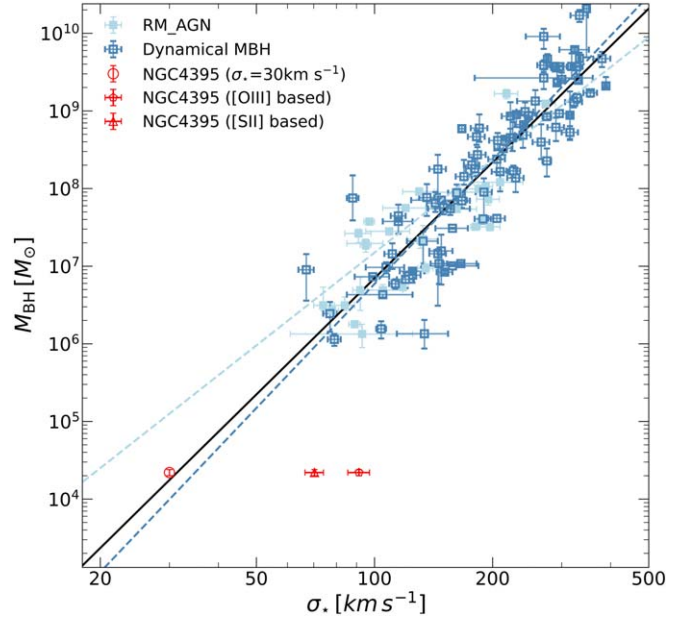

Figure 7. NGC 4395 is plotted on the black hole mass (M_{BH}) vs. stellar velocity dispersion ($\sigma_\star$) diagram. The dynamically measured black hole masses and $\sigma_\star$ for inactive galaxies are in dark blue open squares, taken from J. Kormendy & L. C. Ho (2013) and J. H. Woo et al. (2015). The RM AGN black hole masses are shown with light blue filled squares, taken from J. H. Woo et al. (2015). The M_{BH} for RM AGNs is based on σ_{line} and the $\sigma_\star$ is also compiled from J. H. Woo et al. (2015). The dark blue and light blue dashed lines are the $M_{BH}-\sigma_\star$ fit for the dynamical M_{BH} of inactive galaxies and RM AGNs, and the solid line illustrates the combined fit for dynamical M_{BH} and RM AGN M_{BH}. The slope and intercept are obtained from J. Kormendy & L. C. Ho (2013) and J. H. Woo et al. (2015), respectively. We plotted the source NGC 4395 with the upper limit of $\sigma_\star$, i.e., 30 km s^{-1}, and measured the [O III]$\lambda5007$ and [S II]$\lambda6732$ dispersion along with our measured $M_{BH} = 2.2^{+0.2}_{-0.2} \times 10^4 M_\odot$.

Appendix
Detrending Light Curves

We performed the detrending of the light curves by fitting a straight line to the continuum and line light curve and then
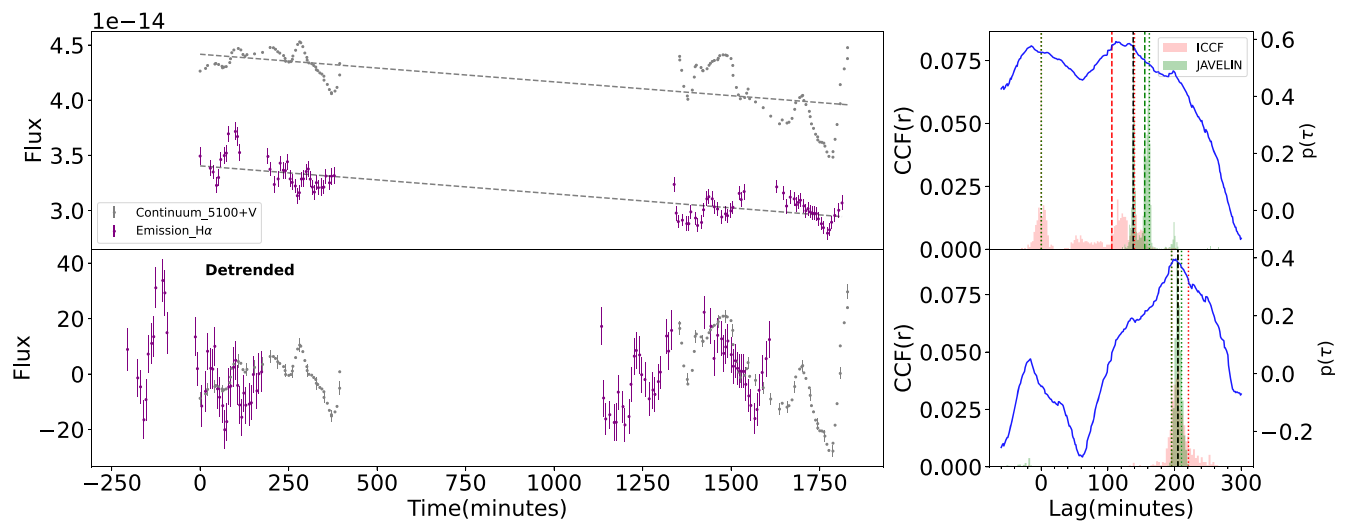
Figure A1. Upper left panel: the continuum and Hα line light curves (arbitrary flux) for the entire two days fitted with a straight line (gray), as mentioned in Section 3.2.2. Lower left panel: the mean-subtracted light curves after detrending are shown. Here, the continuum light curve is normalized, and the emission-line light curve is shifted by a lag of 205 minutes. Right panels: the CCF coefficient (r) along with ICCF and JAVELIN lag histograms before (upper right) and after (lower right) detrending.

subtracting the best-fit straight line to get the detrended light curves, as mentioned in Section 3.2.2. In Figure A1, we showed the light curve and lag results before and after detrending for the entire campaign as an example.

ORCID iDs

Shivangi Pandey ● https://orcid.org/0000-0002-4684-3404
Suvendu Rakshit ● https://orcid.org/0000-0002-8377-9667
C. S. Stalin ● https://orcid.org/0000-0002-4998-1861
Hojin Cho ● https://orcid.org/0000-0003-2010-8521
Jong-Hak Woo ● https://orcid.org/0000-0002-8055-5465
Amit Kumar Mandal ● https://orcid.org/0000-0001-9957-6349

References

Abuter, R., Allouche, F., Amorim, A., et al. 2024, Natur, 627, 281
Amorim, A., Bauböck, M., Bentz, M. C., et al. 2021, A&A, 654, A85
Barbary, K. 2016, JOSS, 1, 58
Barth, A. J., Bennert, V. N., Canalizo, G., et al. 2015, ApJS, 217, 26
Bentz, M. C., Denney, K. D., Grier, C. J., et al. 2013, ApJ, 767, 149
Bentz, M. C., Horenstein, D., Bazhaw, C., et al. 2014, ApJ, 796, 8
Bentz, M. C., Walsh, J. L., Barth, A. J., et al. 2010, ApJ, 716, 993
Beroiz, M., Cabral, J. B., & Sanchez, B. 2020, A&C, 32, 100384
Bontà, E. D., Peterson, B. M., Bentz, M. C., et al. 2020, ApJ, 903, 112
Boroson, T. A., & Green, R. F. 1992, ApJS, 80, 109
Brok, M. d., Seth, A. C., Barth, A. J., et al. 2015, ApJ, 809, 101
Brum, C., Diniz, M. R., Riffel, R. A., et al. 2019, MNRAS, 486, 691
Cackett, E. M., Bentz, M. C., & Kara, E. 2021, iSci, 24, 102557
Cameron, D. T., McHardy, I., Dwelly, T., et al. 2012, MNRAS, 422, 902
Carson, D. J., Barth, A. J., Seth, A. C., et al. 2015, AJ, 149, 170
Cho, H., Woo, J.-H., Hodges-Kluck, E., et al. 2020, ApJ, 892, 93
Cho, H., Woo, J.-H., Treu, T., et al. 2021, ApJ, 921, 98
Cho, H., Woo, J.-H., Wang, S., et al. 2023, ApJ, 953, 142
Desroches, L.-B., Filippenko, A. V., Kaspi, S., et al. 2006, ApJ, 650, 88
Dietrich, M., Peterson, B. M., Grier, C. J., et al. 2012, ApJ, 757, 53
DiRenzo, S., Richardson, C., Lebouteiller, V., Polimera, M., & Kannappan, S. 2024, AAS Meeting Abstracts, 56, 203.01
Du, P., Hu, C., Lu, K. X., et al. 2014, ApJ, 782, 45
Du, P., Hu, C., Lu, K. X., et al. 2015, ApJ, 806, 22
Du, P., Lu, K.-X., Zhang, Z.-X., et al. 2016, ApJ, 825, 126
Du, P., Zhang, Z.-X., Wang, K., et al. 2018, ApJ, 856, 6
Edelson, R., Gelbord, J., Cackett, E., et al. 2019, ApJ, 870, 123
Edri, H., Rafter, S. E., Chelouche, D., Kaspi, S., & Behar, E. 2012, ApJ, 756, 73
Fausnaugh, M. M. 2017, PASP, 129, 024007
Fausnaugh, M. M., Grier, C. J., Bentz, M. C., et al. 2017, ApJ, 840, 97
Feng, H.-C., Liu, H. T., Bai, J. M., et al. 2021, ApJ, 912, 92
Filippenko, A. V., & Ho, L. C. 2003, ApJL, 588, L13
Fitzpatrick, E. L. 1999, PASP, 111, 63
Gaia Collaboration 2020, yCat, I/350, 0
Gonzalez-Buitrago, D. H., Garcia-Diaz, M. T., Pozo Nuñez, F., & Guo, H. 2023, MNRAS, 525, 4524
GRAVITY Collaboration, Amorim, A., Brandner, W., et al. 2020, A&A, 643, 24
Gravity Collaboration, Sturm, E., Dexter, J., et al. 2018, Natur, 563, 657
Greene, J. E., & Ho, L. C. 2004, ApJ, 610, 722
Greene, J. E., & Ho, L. C. 2007, ApJ, 670, 92
Greene, J. E., Strader, J., & Ho, L. C. 2020, ARA&A, 58, 257
Grier, C. J., Trump, J. R., Shen, Y., et al. 2017, ApJ, 851, 21
Gu, H., Wu, X.-B., Wen, Y., Ma, Q., & Guo, H. 2024, MNRAS, 530, 3578
Guo, H. 2023, legolason/PyQSOFit, https://github.com/legolason/PyQSOFit
Guo, H., Barth, A. J., & Wang, S. 2022, ApJ, 940, 20
Guo, H., Liu, X., Shen, Y., et al. 2019, MNRAS, 482, 3288
Guo, H., Shen, Y., & Wang, S., 2018 PyQSOFit: Python Code to Fit the Spectrum of Quasars, Astrophysics Source Code Library, ascl:1809.008
Hu, C., Li, S.-S., Yang, S., et al. 2021, ApJS, 253, 20
Hu, J. 2008, MNRAS, 386, 2242
Kaspi, S., Brandt, W. N., Maoz, D., et al. 2007, ApJ, 659, 997
Kaspi, S., Smith, P. S., Netzer, H., et al. 2000, ApJ, 533, 631
Kelly, B. C., Bechtold, J., & Siemiginowska, A. 2009, ApJ, 698, 895
Kelly, B. C., Becker, A. C., Sobolewska, M., Siemiginowska, A., & Uttley, P. 2014, ApJ, 788, 33
Kokorev, V., Fujimoto, S., Labbe, I., et al. 2023, ApJL, 957, L7
Kollatschny, W., & Zetzl, M. 2011, Natur, 470, 366
Kormendy, J., & Ho, L. C. 2013, ARA&A, 51, 511
Kraemer, S. B., Ho, L. C., Crenshaw, D. M., Shields, J. C., & Filippenko, A. V. 1999, ApJ, 520, 564
Kumar, B., Omar, A., Maheswar, G., et al. 2018, BSRSL, 87, 29
La Franca, F., Onori, F., Ricci, F., et al. 2015, MNRAS, 449, 1526
Latif, M. A., Schleicher, D. R. G., Schmidt, W., & Niemeyer, J. C. 2013, MNRAS, 436, 2989
Le, H. A. N., Xue, Y., Lin, X., & Wang, Y. 2023, ApJ, 945, 59
Li, S.-S., Feng, H.-C., Liu, H. T., et al. 2022, ApJ, 936, 75
Li, S.-S., Yang, S., Yang, Z.-X., et al. 2021, ApJ, 920, 9
Li, Y.-R. 2024, PyCALI: A Bayesian Package for Intercalibrating Light Curves (v0.2.3), Zenodo, doi:10.5281/zenodo.10700132
Li, Y.-R., Wang, J.-M., Hu, C., Du, P., & Bai, J.-M. 2014, ApJL, 786, L6
Loeb, A., & Rasio, F. A. 1994, ApJ, 432, 52
Malik, U., Sharp, R., Penton, A., et al. 2023, MNRAS, 520, 2009

McHardy, I. M., Beard, M., Breedt, E., et al. 2023, MNRAS, 519, 3366
McHardy, I. M., Koerding, E., Knigge, C., Uttley, P., & Fender, R. P. 2006, Natur, 444, 730
Mezcua, M. 2017, IJMPD, 26, 1730021
Montano, J. W., Guo, H., Barth, A. J., et al. 2022, ApJL, 934, L37
Mushotzky, R. F., Edelson, R., Baumgartner, W., & Gandhi, P. 2011, ApJL, 743, L12
National Optical Astronomy Observatories, 1999 Image Reduction and Analysis Facility, Astrophysics Source Code Library, ascl:9911.002
Omar, A., Kumar, T. S., Krishna Reddy, B., Pant, J., & Mahto, M. 2019, CSci, 116, 1472
Onken, C. A., Ferrarese, L., Merritt, D., et al. 2004, ApJ, 615, 645
Panchal, D., Kumar, T. S., Omar, A., & Misra, K. 2023, JATIS, 9, 018002
Pandey, S., Rakshit, S., Woo, J.-H., & Stalin, C. S. 2022, MNRAS, 516, 2671
Park, S., Woo, J.-H., Romero-Colmenero, E., et al. 2017, ApJ, 847, 125
Pei, L., Fausnaugh, M. M., Barth, A. J., et al. 2017, ApJ, 837, 131
Peng, C. Y., Ho, L. C., Impey, C. D., & Rix, H.-W. 2002, AJ, 124, 266
Peng, C. Y., Ho, L. C., Impey, C. D., & Rix, H.-W. 2010, AJ, 139, 2097
Peterson, B. M. 1993, PASP, 105, 247
Peterson, B. M. 2014, SSRv, 183, 253
Peterson, B. M., Bentz, M. C., Desroches, L., et al. 2005, ApJ, 632, 799
Peterson, B. M., Berlind, P., Bertram, R., et al. 2002, ApJ, 581, 197
Peterson, B. M., Ferrarese, L., Gilbert, K. M., et al. 2004, ApJ, 613, 682
Peterson, B. M., Grier, C. J., Horne, K., et al. 2014, ApJ, 795, 149
Peterson, B. M., Wanders, I., Bertram, R., et al. 1998, ApJ, 501, 82
Rafter, S. E., Kaspi, S., Behar, E., Kollatschny, W., & Zetzl, M. 2011, ApJ, 741, 66
Rakshit, S. 2020, A&A, 642, A59
Rakshit, S., Stalin, C. S., & Kotilainen, J. 2020, ApJS, 249, 17
Rakshit, S., Woo, J.-H., Gallo, E., et al. 2019, ApJ, 886, 93
Reines, A. E., Greene, J. E., & Geha, M. 2013, ApJ, 775, 116
Rodriguez-Pascual, P. M., Alloin, D., Clavel, J., et al. 1997, ApJS, 110, 9
Sagar, R., Omar, A., Kumar, B., et al. 2011, CSci, 101, 1020
Schlegel, D. J., Finkbeiner, D. P., & Davis, M. 1998, ApJ, 500, 525
Sergeev, S. G., Nazarov, S. V., & Borman, G. A. 2016, MNRAS, 465, 1898
Sexton, R. O., Matzko, W., Darden, N., Canalizo, G., & Gorjian, V. 2021, MNRAS, 500, 2871
Shen, Y., Hall, P. B., Horne, K., et al. 2019, A&AS, 241, 34
Shin, L., Woo, J.-H., Son, D., et al. 2022, AJ, 163, 73
Tody, D. 1986, Proc. SPIE, 627, 733
Tody, D. 1993, in ASP Conf. Ser. 52, Astronomical Data Analysis Software and Systems II, ed. R. J. Hanisch, R. J. V. Brissenden, & J. Barnes (San Francisco, CA: ASP), 173
U, V., Barth, A. J., Vogler, H. A., et al. 2022, ApJ, 925, 52
van Dokkum, P. G. v. 2001, PASP, 113, 1420
Ward, C., Gezari, S., Nugent, P., et al. 2022, ApJ, 936, 104
Welsh, W. F. 1999, PASP, 111, 1347
Williams, P. R., Pancoast, A., Treu, T., et al. 2020, ApJ, 902, 74
Woo, J.-H., Cho, H., Gallo, E., et al. 2019, NatAs, 3, 755
Woo, J.-H., Schulze, A., Park, D., et al. 2013, ApJ, 772, 49
Woo, J.-H., Wang, S., Rakshit, S., et al. 2024, ApJ, 962, 67
Woo, J. H., Yoon, Y., Park, S., Park, D., & Kim, S. C. 2015, ApJ, 801, 1
Yang, X., Mohan, P., Yang, J., et al. 2022, ApJ, 941, 43
Yu, Z., Kochanek, C. S., Peterson, B. M., et al. 2020, MNRAS, 491, 6045
Zhang, X.-G., Dultzin-Hacyan, D., & Wang, T.-G. 2007, MNRAS, 374, 691
Zhang, Z.-X., Du, P., Smith, P. S., et al. 2019, ApJ, 876, 49
Zu, Y., Kochanek, C. S., Kozłowski, S., et al. 2013, ApJ, 765, 106
Zu, Y., Kochanek, C. S., & Peterson, B. M. 2011, ApJ, 735, 80